48th AIAA Aerospace Sciences Meeting Including the New Horizons Forum and Aerospace Exposition
4 - 7 January 2010, Orlando, Florida

AIAA 2010-966

Three-dimensional Plasma and Fluid Flow Structures inside a Microscale Electrohydrodynamic Pump

Chin-Cheng Wang* and Subrata Roy§
Computational Plasma Dynamics Laboratory and Test Facility
Mechanical and Aerospace Engineering Department
University of Florida, Gainesville, FL 32611-6300

Dielectric barrier discharge (DBD) is simulated in three dimensions using the finite element based multiscale ionized gas (MIG) flow code. Two-species hydrodynamic plasma model coupled Poisson equation and Navier-Stokes equation are solved using MIG flow code to predict complicated flow structure inside a plasma induced micropump. The advantage of such micropump is rapid on/off switching without any moving parts. Results show reasonable distribution for ion and electron densities as well as an electric field. The key factors of design of plasma micropump are location of actuators and input voltage. The flow rate of plasma micropump is on the order of ml/min. Such flow rate may be beneficial for many applications from biological analysis to micropropulsion in space.

Nomenclature

c	=	speed of sound (m/s)
D_e	=	electron diffusion coefficient (cm^2/s)
D_i	=	ion diffusion coefficient (cm^2/s)
E	=	electric field (V/m)
e	=	elementary charge (C)
F	=	electric force density (N/m^3)
k_B	=	Boltzmann's constant (J/K)
n_e	=	electron density (m^{-3})
n_i	=	ion density (m^{-3})
p	=	pressure (Torr) or (Pa)
Q	=	flow rate (ml/min)
q	=	charge density, (n_i-n_e) (m^{-3})
r	=	electron-ion recombination rate (cm^3/s)
T_e	=	electron temperature (K) or (eV)
T_i	=	ion temperature (K) or (eV)
V_e	=	electron velocity (m/s)
V_i	=	ion velocity (m/s)
V_n	=	nitrogen velocity (m/s)
α	=	Townsend coefficient (cm^{-1})
ε	=	dielectric constant (Farad/m)
ϕ	=	potential (V)
Λ	=	macroscopic characteristic length (m)
λ	=	mean free path (m)
μ_e	=	electron mobility (cm^2/sV)
μ_i	=	ion mobility (cm^2/sV)
ρ	=	fluid density (kg/m^3)

* Research Scientist, Member AIAA, james614@ufl.edu
§ Associate Professor, Associate Fellow AIAA, roy@ufl.edu

I. Introduction

The mircopump is made by fabrication on the order of micrometers to draw or drain the working fluid in the microfluidic system, such as lab-on-a-chip (LOC) or a micro total analysis system (μTAS). Since its introduction in mid 1970s,[1] micropumps are becoming widely popular in a variety of applications ranging from biological analysis and chemical detection to space exploration and microelectronics cooling. A variety of micropumps has been developed based on the operational mechanism. These may be categorized as mechanical and non-mechanical devices. Mechanical micropumps drive the working fluid through a membrane or diaphragm, while non-mechanical micropumps inject momentum or energy into a local region to produce pumping operation. Based on the motion of mechanical micropumps, it can be divided into reciprocating, rotary, and aperiodic pumps. Mechanical micropumps include electrostatic, pneumatic, thermopneumatic, piezoelectric, and electromagnetic diaphragm pumps. Diaphragm pumps can be used for any gas or liquid and generate flow rates in the range of ml/min. However, the drawbacks are the relatively high cost and the short life time of moving diaphragm due to their frequently on/off switching. In contrast, the primary advantage of non-mechanical micropumps is without moving parts. Furthermore, the simple design of such pumps may reduce the cost and increase miniaturization, so that it improves the integration into the microfluidic system. Non-mechanical micropumps include electro-hydrodynamic (EHD), electroosmotic, and magnetohydrodynamic pumps. A thorough review of the actuation mechanism and the applications of micropumps have been described by Laser, Santiago, Oh, and Ahn.[2-3]

Roy[4] presented a concept of EHD micropump using dielectric barrier discharge (DBD) actuators shown in figure 1. Such design leverage several advantages of non-mechanical micropumps. Over the last decade, many experiments and numerical simulation show that DBD actuators produce effects on drag reduction inside the boundary layer.[5-9] However, these traditional macroscale DBD actuators suffer from relatively small actuation at high speed flow (> 30 m/s). As a remedy, microscale plasma actuators may induce orders of magnitude higher force density.[10]

Microscale plasma discharge has been studied both experimentally and numerically for more than a decade.[10-20] However, there is still room for understanding of the fundamental physics in reduced length scale, the unsteady phenomena, and the interaction between plasma and gas in micro gap. Several numerical investigations of microscale discharge generally fall into three major categories: (1) Hydrodynamic model, which is based on conservation of mass and momentum.[14-17] (2) Kinetic model, which is the particle-in-cell/Monte Carlo collision (PIC/MCC) model.[18-19] (3) Hybrid kinetic-fluid simulation model, which solves the reaction rates from Monte Carlo collision model and then bring the solutions into the hydrodynamic model to get the plasma physics.[20] In this paper, we choose the hydrodynamic model which is the most popular due to its effective capturing of the overall physics at a low computational cost.

Our recent two-dimensional hydrodynamic model of microscale direct current (DC) volume discharge[10] shows very good agreement with published experimental data. The results mimic trend at both macro and microscale discharge, but the sheath structure dominated the plasma region at certain value of micro gap. The force density is also found to be three orders of magnitude higher than the macro plasma actuator. However, the net flow inducement remains similar to that of standard actuator due to orders of magnitude smaller plasma region than the traditional counterparts. A two-dimensional plasma micropump model was simulated for the plasma-gas interactions predicting a reasonable 28.5 ml/min flow rate of nitrogen gas. However, such 2D models are limited especially for a 3D geometry. Thus, for a better design of the plasma micropump, it is important to identify three-dimensional effects on plasma and gas flow fields. To our knowledge, the reported numerical results of plasma simulation are either one- or two- dimensional. So far, very little work has been done on plasma micropump in three-dimensional simulation.

In this paper, we extend our two-dimensional hydrodynamic model[8, 10, 21] into the three-dimensional pulsed dc plasma simulation. The ion density, electron density, and electric field will be solved based on first-principles. The obtained electric force density ($F = eqE$) from plasma simulation will be employed as a local body force term in the Navier-Stokes equation. Section II provides the governing equations for plasma and fluid flow. Section III describes the finite element method (FEM) based multiscale ionized gas (MIG) flow code. Section IV gives two

different designs of plasma micropumps. Section V shows results of plasma micropumps for two cases. Conclusions are summarized in the section VI.

II. Numerical Model

We extend the two-dimensional two-species hydrodynamic plasma formulation of Kumar and Roy[21] into a three-dimensional model for plasma micropump simulation. The unsteady transport for ions and electrons is derived from the first principles in the form of conservation of species continuity. The species momentum flux embedded in them using the drift-diffusion approximation under isothermal condition. Such approximation can predict general characteristics of plasma discharges in the pressure range from 1 to 50 Torr.[22] The continuity equations for concentration of positive ion n_i and electron n_e together with Poisson equation for electric field vector $\mathbf{E}$ (E_x, E_y, E_z):

$$\begin{aligned}
&\frac{\partial n_i}{\partial t} + \nabla \cdot \left(n_i \mathbf{V}_i \right) = \alpha \left| \Gamma_e \right| - r n_i n_e \\
&\frac{\partial n_e}{\partial t} + \nabla \cdot \left(n_e \mathbf{V}_e \right) = \alpha \left| \Gamma_e \right| - r n_i n_e \\
&\left| \Gamma_e \right| = \sqrt{(n_e V_e)_x^2 + (n_e V_e)_y^2 + (n_e V_e)_z^2} \\
&\nabla \cdot (\varepsilon \mathbf{E}) = -e(n_e - n_i)
\end{aligned} \qquad (1)$$

where n_e and n_i are number densities of electron and ion respectively, $\mathbf{V}$ (V_x, V_y, V_z) is the species hydrodynamic velocity, $r \sim 2\times10^{-7}$ cm^3/s is the electron-ion recombination rate, ε is the dielectric constant, the elementary charge e is 1.6022×10^{-19} C, and subscript i and e are positive ion and electron, respectively. The working gas is nitrogen at 5 Torr. The discharge is maintained using a Townsend ionization scheme. The ionization rate is expressed as a function of electron drift velocity $\left|\Gamma_e\right|$ and Townsend coefficient α:

$$\alpha = Ap \exp\left(-B/(|\mathbf{E}|/p)\right) \qquad (2)$$

where A = 12 (cm Torr)$^{-1}$ and B = 342 V/(cm Torr) are preexponential and exponential constants, respectively, p is the gas pressure, and E is the electric field. The ionic and electronic fluxes in equation (1) are written as:

$$\begin{aligned}
&n_i \mathbf{V}_i = n_i \mu_i \left(\mathbf{E} + \mathbf{V}_i \times \mathbf{B} \right) - D_i \nabla n_i \\
&n_e \mathbf{V}_e = -n_e \mu_e \left(\mathbf{E} + \mathbf{V}_e \times \mathbf{B} \right) - D_e \nabla n_e
\end{aligned} \qquad (3)$$

The Lorentz force term, $\mathbf{V}\times\mathbf{B}$, brings in the effect of the magnetic field $\mathbf{B}$. We set $\mathbf{B} = 0$ to neglect the magnetic field effect. Finally, we end up with the following equations:

$$\begin{aligned}
&\frac{\partial n_i}{\partial t} + \frac{\partial}{\partial x}\left\{ n_i \mu_i E_x - D_i \frac{\partial n_i}{\partial x} \right\} + \frac{\partial}{\partial y}\left\{ n_i \mu_i E_y - D_i \frac{\partial n_i}{\partial y} \right\} + \frac{\partial}{\partial z}\left\{ n_i \mu_i E_z - D_i \frac{\partial n_i}{\partial z} \right\} = \alpha \left| \Gamma_e \right| - r n_i n_e \\
&\frac{\partial n_e}{\partial t} + \frac{\partial}{\partial x}\left\{ -n_e \mu_e E_x - D_e \frac{\partial n_e}{\partial x} \right\} + \frac{\partial}{\partial y}\left\{ -n_e \mu_e E_y - D_e \frac{\partial n_e}{\partial y} \right\} + \frac{\partial}{\partial z}\left\{ -n_e \mu_e E_z - D_e \frac{\partial n_e}{\partial z} \right\} = \alpha \left| \Gamma_e \right| - r n_i n_e
\end{aligned} \qquad (4)$$

where $\mu_i = 1.45\times10^3 / p$ (cm^2/sV) is the ion mobility, $\mu_e = 4.4\times10^5 / p$ (cm^2/sV) is the electron mobility, D_i and D_e are the ion and electron diffusion coefficients calculated from the Einstein relation which is a function of ion and electron mobility as well as ion and electron temperature, i.e. $D_i = \mu_i T_i$ and $D_e = \mu_e T_e$. The electric field is given by $E = -\nabla\varphi$, i.e., the gradient of electric potential φ. The system of equation (1) is normalized using the following normalization scheme: $\tau = t/t_0$, $z_i = x_i/d$, $N_e = n_e/n_0$, $N_i = n_i/n_0$, $u_e = V_e/V_B$, $u_i = V_i/V_B$, and $\phi = e\varphi/k_B T_e$ where k_B is Boltzmann's constant, $V_B = \sqrt{k_B T_e / m_i}$ is the Bohm velocity, reference length d which is usually a domain characteristic length in the geometry, the reference time $t_0 = 10^{-8}$ second, and reference density $n_0 = 10^{15}$ m^{-3}.

Nitrogen gas is governed by the conservation of mass as:

$$\frac{\partial \rho}{\partial t} + \nabla \cdot (\rho \mathbf{V_n}) = 0 \qquad (5)$$

where ρ is the fluid density and subscript n denotes the working nitrogen gas. The second term can be further decomposed via chain rule:

$$\frac{\partial \rho}{\partial t} + \mathbf{V_n} \cdot \nabla \rho + \rho \nabla \cdot \mathbf{V_n} = \frac{D\rho}{Dt} + \rho \nabla \cdot \mathbf{V_n} = 0 \qquad (6)$$

For incompressible flow, the characteristic velocity $\mathbf{V_n}$ must be much smaller than the speed of sound c, i.e. Mach numbers Ma = $\mathbf{V_n}$ / c below approximately 0.3, and the compressible effect can be neglected. For the incompressible fluid (ρ = constant, $D\rho/Dt = 0$) is $\nabla \cdot \mathbf{V_n} = 0$.

The conservation of momentum may be drived from Newton's second law as follows:

$$\rho \frac{D\mathbf{V_n}}{Dt} = \rho \mathbf{F} + \nabla \cdot \boldsymbol{\sigma} \qquad (7)$$

where $\mathbf{F} = eq\mathrm{E}$ is the body force and $\boldsymbol{\sigma} = -\nabla p + \mu \nabla^2 \mathbf{V_n}$ is the stress tensor, where p is the pressure, and μ is the viscosity of fluid. For an incompressible Newtonian fluid, the Navier-Stokes equation is:

$$\rho \frac{D\mathbf{V_n}}{Dt} = \rho \mathbf{F} - \nabla p + \mu \nabla^2 \mathbf{V_n} \qquad (8)$$

In the microscale regime, the continuum approach with the no-slip boundary condition may not hold when the Knudsen number is greater than 0.1 shown in table 1. The non-dimensional Knudsen number is defined as the ratio of the fluid mean free path λ and macroscopic characteristic length Λ, i.e. Kn = λ / Λ. As Kn increases, the rarefaction effects become more dominant between the bulk of the fluid and the wall surface. For conditions stated in this paper, the Kn is less than 0.024 validating the use of no-slip condition.

Table 1. Different regimes of fluid flow depending on the Knudsen number.[23]

Range, Kn	Flows	Equations
$0 \sim 10^{-2}$	Continuum flow	No-slip Navier-Stokes
$10^{-2} \sim 10^{-1}$	Slip flow	Slip Navier-Stokes
$10^{-1} \sim 10^{1}$	Transition flow	Burnett equations
$10^{1} \sim \infty$	Free-molecule flow	Boltzmann equations

The numerical model for solving DBD plasma and Navier-Stokes equations uses an efficient finite element algorithm for solving partial differential equations (PDE) approximately. The solution methodology anchored in the modular MIG flow code is based on the Galerkin Weak Statement (GWS) of the PDE[24-25] which is derived from variational principles. An iterative sparse matrix solver called Generalized Minimal RESidual (GMRES) is utilized to solve the resultant stiff matrix. The fully implicit time stepping procedure along with the Newton-Raphson scheme is used for dealing with this nonlinear problem. The solution is assumed to have converged when the L_2 norms of all the normalized solution variables and residuals are below a chosen convergence criterion of 10^{-3}.

III. Problem description

Figure 2 shows a schematic of plasma micropump of Case#1 for (A) cross-section and (B) isometric view. We can see this tri-directional plasma pump draws the fluid into the micro channel at the both inlets due to the attraction of parallel plasma actuators and drains the fluid upward to the outlet by means of horseshoe plasma actuators. Two cases described in table 2 were simulated. The inlet openings of the pump for both cases are 0.1296 mm^2, while the outlet openings are 0.24 mm^2 for Case#1 and 0.39 mm^2 for Case#2. The volume of plasma micropump is 2 mm^3. The length and width of the electrodes are 200 μm and 12.5 μm for the parallel actuator. The horseshoe actuator consists of two semi-circle electrodes with inner arc radius of 0.25 μm. We neglect the thickness of the electrodes in vertical *z*-direction. The gap between electrodes is 50 μm in streamwise *x*-direction and 24 μm in vertical *z*-direction which is also the dielectric thickness. We only simulate the symmetric half of these plasma micropumps to reduce computational cost.

Table 2. Geometric parameter for Case#1 and Case#2.

Unit: μm	l_1	l_2	l_3	h_1	h_2	w
Case#1	1000	400	1000	216	144	600
Case#2	875	650	875	216	144	600

Figure 3 shows the computational mesh in two-dimensional cross-section and three-dimensional domain for Case#1 and Case#2. The domain size consists of 96x48x60 tri-linear elements with 289,933 nodes. The mesh density is on the order of Debye length which is sufficient to capture the physics of plasma dynamics. Figure 3(A) shows the locations of all the actuators in a two-dimensional cross-section for Case#1. The powered electrodes (red color) are from x = 0.25 to 0.2625 mm, from x = 0.6 to 0.6125 mm, and from x = 1.375 to 1.5 mm. The dielectric surface is Teflon film between electrodes from z = 0 to 0.024 mm and from z = 0.216 to 0.24 mm. The grounded electrodes (black color) are from x = 0.3125 to 0.325 mm, from x = 0.6625 to 0.675 mm, and from x = 0.975 to 0.9875 mm. The mesh densities of Case#2 and Case#1 are same shown in figure 3(B), but the location of the actuators and the size of outlet opening are different. For the plasma boundary conditions, pulsed dc potential is applied to powered electrode of $\phi = \phi_0 \sin^4(2\pi f t)$ volts. We have chosen ϕ_0 = 50 V and f = 5 kHz for Case#1 and ϕ_0 = 80 V and f = 5 kHz for Case#2. For the fluid flow boundary conditions, we assume zero pressure (p = 0) at inlet and outlet and no-slip condition on the dielectric surface for all three velocity components V_x, V_y, and V_z. We assume symmetric boundary condition at x = 1.2 mm which is the center of the plasma micropump.

IV. Results and Discussion

Two different outlet openings and applied potential of plasma micropumps are simulated. The results at peak potential ϕ_0 for Case#1 are shown in figures 4-5, while the results for Case#2 are shown in figure 6-7. For plasma simulation, ion and electron densities are solved using two-species hydrodynamic model coupled with Poisson equation. The ion and electron are formed through ionization process. The recombination is also considered for the time averaged ion and electron densities. Due to the large time scale difference between plasma and fluid flow, we only consider the plasma actuation on the fluid.

A. Case#1

Figure 4 shows the charge separation at y = 0.3 mm and potential contour plot at z = 0.03 mm with force vectors. The charge separation is given by $q = n_i - n_e$ shown in figure 4(A). The peak of charge separation is close to the powered electrode. The strongest force vectors is also close to the powered electrode because the time average of electrostatic force per volume ($\mathbf{F} = eq\mathbf{E}$) is function of charge separation and electric field. We also can see that the force vectors are acting from the powered electrode to the grounded electrode which is matching electric field lines

shown. Potential distribution is solved by Poisson equation and matches the boundary condition from 50 V to 0 V shown in figure 4(B).

The reasonable time averaged electric force density is solved by plasma simulation. This force density is the body source term in the Navier-Stokes equation to actuate the fluid flow shown in figure 5. Figure 5(A) shows that the electric force draws the fluid from inlet at left and drains the fluid upward to the outlet at top. The contour is colored by V_z-velocity component and shows the highest upward velocity close to the corner of the plasma micropump. We can see a vortex at right boundary (symmetric plane) because the horseshoe actuator sucks the fluid from top and pushes it from right to left and creates a plasma barrier. Figure 5(B) shows the streamwise flow hits this plasmas barrier at x = 0.8 mm. Figure 5(A) shows two vortical structures at inlet which were not found in our two-dimensional simulation.[10] This is because we assume that the electrode is infinite long at the third direction for two-dimensional simulation. In the three-dimensional case, we need to consider the wall effect at the *y*-direction shown in figure 5(B).

B. Case#2

Figure 6 shows the charge separation and potential distribution with force vectors for Case#2. We can see the highest value of the charge separation increase due to the potential increase. The force vectors are still acting toward the grounded electrode due to the distribution of electric field and charge separation. For the Case#2, the highest applied voltage is 80 V which is matching the given boundary conditions shown in figure 6(B).

Figure 7 shows the fluid streamtraces at (A) y = 0.3 mm and (B) z = 0.12 mm. Figure 7(A) shows that the inlet vortices shown in figure 5(A) have been reduced due to the higher electric force than Case#1. Also, the location of the actuators may be another factor. However, we can see a bigger vortical structure at the outlet because the horseshoe plasma actuator sucks more fluid from the outlet and pushes it back to the outlet and creates a clockwise vortical structure. Figure 7(B) shows the fluid moves right along the *x*-direction and hits this clockwise plasma barrier at x = 0.85 mm. So the fluid has to alter the flow direction upward. It is obvious that the flow of Case#2 is better than Case#1 due to the fewer vortices inside the plasma micropump.

Figure 8 shows the comparison of fluid particles colored by velocity magnitude for (A) Case#1 and (B) Case#2 in isometric view. The top wall is colored by the velocity magnitude, while the bottom wall is colored by the potential. So we can easily see the outlet and the location of the actuators. The velocity magnitude of particles for Case#2 (red) is much faster than that in Case#1 (near blue). Also, the streamtraces of fluid flow are smoother than Case#1. For the calculation of average flow rate Q, we find Q_1 = 0.63 ml/min and Q_2 = 1.5 ml/min. Importantly, the predicted flow rate Q for the designs of Case#1 and Case#2 are one order of magnitude higher than the design reported in literature[2] for the same level of input voltage.

V. Conclusion

We have studied two cases of plasma micropumps using two-species three-dimensional hydrodynamic plasma model coupled with Possion equation. Both plasma governing equation and Navier-Stokes equation are solved using a three-dimensional finite element based multiscale ionized gas (MIG) flow code. The results show the highest charge separation and force close to the powered electrodes. We find three vortical structures inside the pump which can not be found in our two-dimensional simulation. To reduce the vortices inside the plasma micropump, the location of the actuators and the input voltage may be key factors. The three-dimensional flow simulation predicts roughly three times lower flow rate (Q_2 = 1.5 ml/min) with 80 volts in Case#2 than that in Case#1 (Q_1 = 0.63 ml/min) with 50 volts. Such flow rates are one order of magnitude higher than that previously reported for the same level of input voltage and may be quite useful for a range of practical applications.

Acknowledgments

This work was partially supported by the AFOSR Grant Nos. FA9550-07-1-0131 and FA9550-09-1-0372 monitored by Drs. John Schmisseur and Doug Smith.

References

[1]Thomas, L. J. and Bessman, S. P., 1975, "Micropump powered by piezoelectric disk benders", US Patent 3963380.

[2]Laser, D. J. and Santiago, J. G., 2004, "A review of micropumps", *J. Micromech. Microeng*. 14, R35–R64.

[3]Oh, K. W. and Ahn, C. H., 2006, "A review of microvalves", *J. Micromech. Microeng.* 16, R13–R39.

[4]Roy, S., 2007, "Method and apparatus for efficient micropumping" International Publication number PCT International Publication WO 2009/015371.

[5]Roth, J. R., Sherman, D. M. and Wilkinson, S. P., 1998, "Boundary layer flow control with a one atmosphere uniform glow discharge surface plasma", 36th AIAA Aerospace Sciences Meeting and Exhibit, AIAA 98-0328.

[6]Corke, T. C., Jumper, E. J., Post, M. L., Orlov, D. and McLaughlin, T. E., 2002, "Application of weakly-ionized plasmas as wing flow-control devices", 40th AIAA Aerospace Sciences Meeting and Exhibit, AIAA-2002-350.

[7]Shyy, W., Jayaraman, B. and Andersson, A., 2002, "Modeling of glow discharge-induced fluid dynamics", *J. Appl. Phys.* 92(11), 6434-6443.

[8]Roy, S. and Gaintonde, D., 2006, "Force interaction of high pressure glow discharge with fluid flow for active separation control", *Phys. Plasmas* 13, 023503.

[9]Roy, S. and Wang, C.-C, 2009, "Bulk fluid modification with horseshoe and serpentine plasma actuator", *J. Phys. D: Appl. Phys.* 42, 032004.

[10]Wang, C.-C, and Roy, S., 2009, "Microscale plasma actuators for improved thrust density", *J. Appl. Phys.* 106, 013310.

[11]Hibbe, L. B., Sichler, P., Schrader, C., Lucas, N., Gericke, K. H. and Buttgenbach, S., 2005 "High frequency glow discharges at atmospheric pressure with micro-structured electrode arrays", *J. Phys. D: Appl. Phys.* 38, 510-517.

[12]Torres, J. M. and Dhariwal, R. S., 1999, "Electric field breakdown at micrometre separations", *Nanotechnology* 10, 102-107.

[13]Massines, F., Gherardi, N., Naude, N., and Segur, P., 2005, "Glow and Townsend dielectric barrier discharge in various atmosphere", *Plasma Phys. Control Fusion* 47, B577–B588.

[14]Kushner, M. J., 2004, "Modeling of microdischarge devices: Pyramidal structures", *J. Appl. Phys*. 95, 3.

[15]Kushner, M. J., 2005, "Modeling of microdischarge devices: plasma and gas dynamics", *J. Phys. D: Appl. Phys*. 38 1633–1643.

[16]Boeuf, J. P., Pitchforda, L. C., and Schoenbach, K. H., 2005, "Predicted properties of microhollow cathode discharges in xenon", *Appl. Phys. Lett.* 86, 071501.

[17]Wang, Q., Economou, D. J. and Donnelly, V. M., 2006, "Simulation of a direct current microplasma discharge in helium at atmospheric pressure", *J. Appl. Phys.* 100, 023301.

[18]Radjenovic, M. R., Lee, J. K., Iza, F. and Park, G. Y., 2005, "In Particle-in-cell simulation of gas breakdown in microgaps", *J. Phys. D: Appl. Phys*. 38, 950–954.

[19]Choi, J., Iza, F., Lee, J. K. and Ryu, C. M., 2007, "Electron and ion kinetics in a DC microplasma at atmospheric pressure" *IEEE Transactions on Plasma Science* 35, 5.

[20]Farouk, T., Farouk, B., Staack, D., Gutsol, A. and Fridman, A., 2006, "Simulation of DC atmospheric pressure argon micro glow-discharge", *Plasma Sources Sci. Technol*. 15, 676–688.

[21]Kumar, H. and Roy, S., 2005, "Multidimensional hydrodynamic plasma-wall model for collisional plasma discharges with and without magnetic field effects", *Phys. Plasmas* 12, 093508.

[22]Surzhikov, S. T. and Shang, J. S., 2004, "Two-component plasma model for two-dimensional glow discharge in magnetic field", *J. Comput. Phys*. 199, 437-464.

[23]Roy, S., Raju, R., Chuang, H. F., Cruden, B. A. and Meyyappan, M., 2003, "Modeling gas flow through microchannels and nanopores", *J. Appl. Phys.* 93, 8.

[24]Carey, G. F. and Oden, J. T., 1981, "Finite elements: a second course - Volume 2", Prentice Hall.

[25]Baker, A. J. and Pepper, D. W., 1991, "Finite element 1-2-3", McGraw Hill Inc.

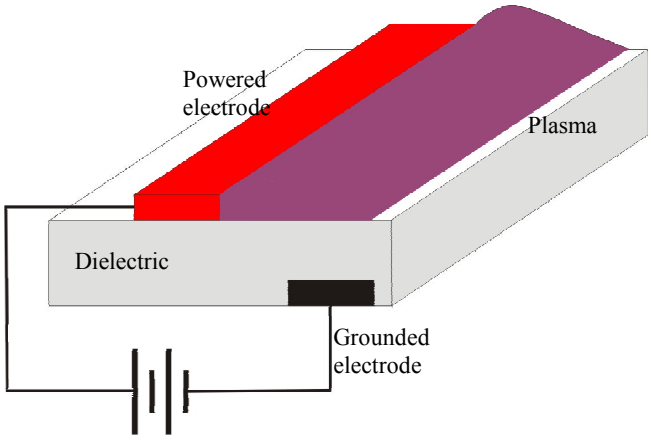

Figure 1. Schematic of the asymmetric single dielectric barrier plasma actuator.

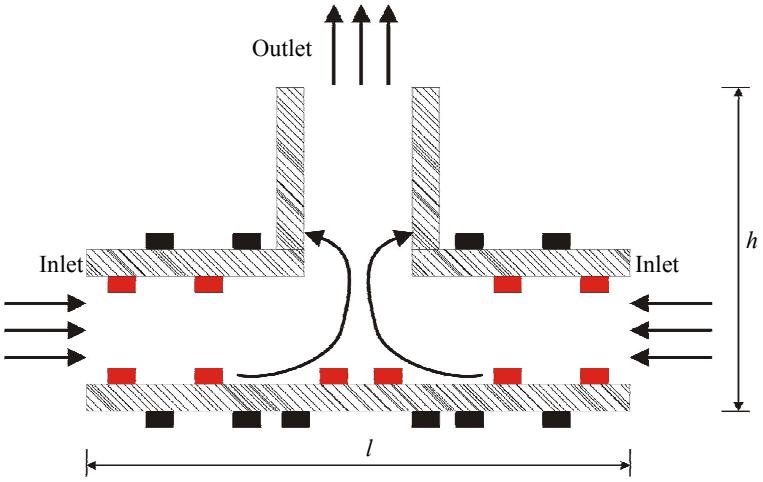

A)

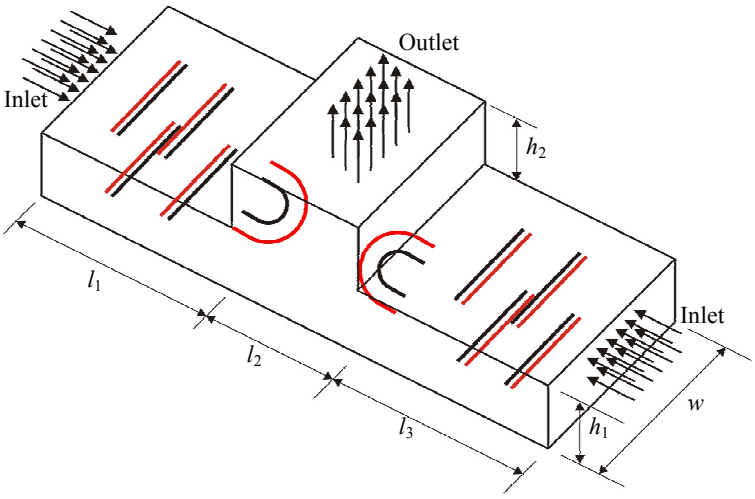

B)

Figure 2. Schematic of plasma micropump for A) cross-section and B) isometric view.

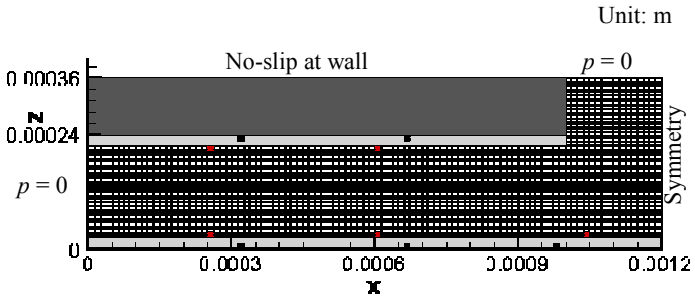

A)

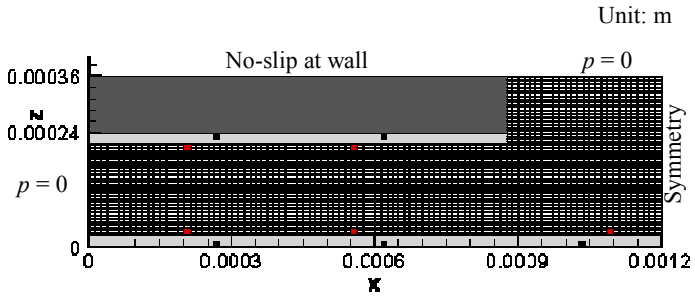

B)

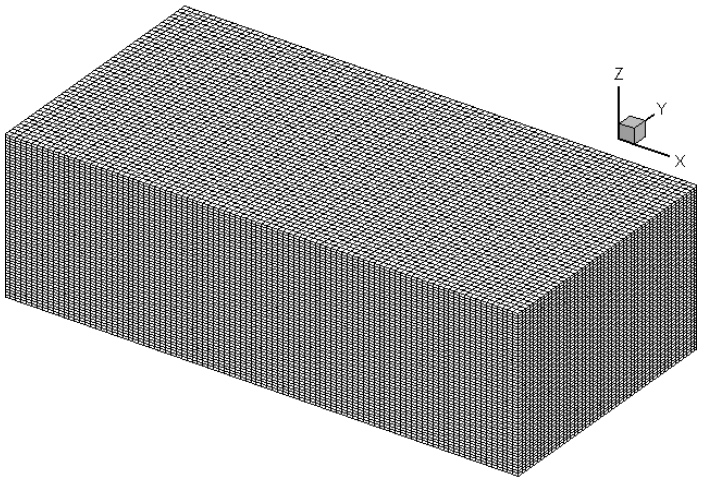

C)

Figure 3. Computational mesh density for A) cross-section of Case#1, B) cross-section of Case#2, and C) isometric view.

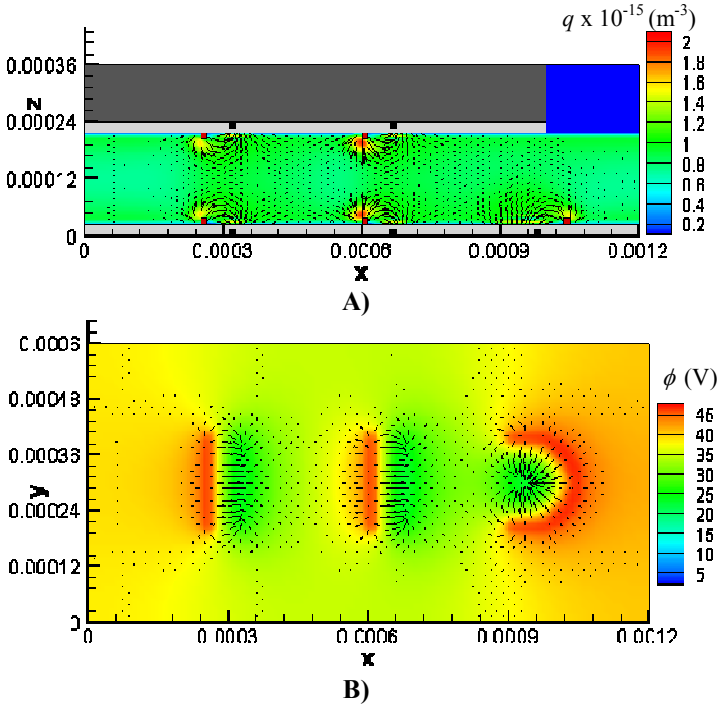

Figure 4. Case#1: A) charge separation $q = n_i - n_e$ at x-z plane (y = 0.3 mm) and B) potential distribution at x-y plane (z = 0.03 mm) with force vectors.

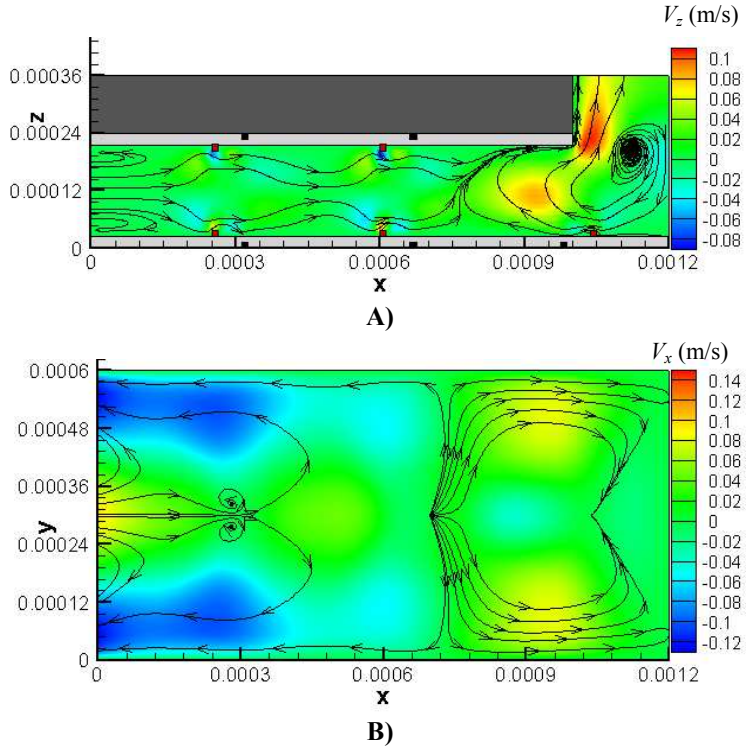

Figure 5. Case#1: A) V_z-velocity contour at x-z plane (y = 0.3 mm) and B) V_x-velocity contour at x-y plane (z = 0.12 mm) with streamtraces.

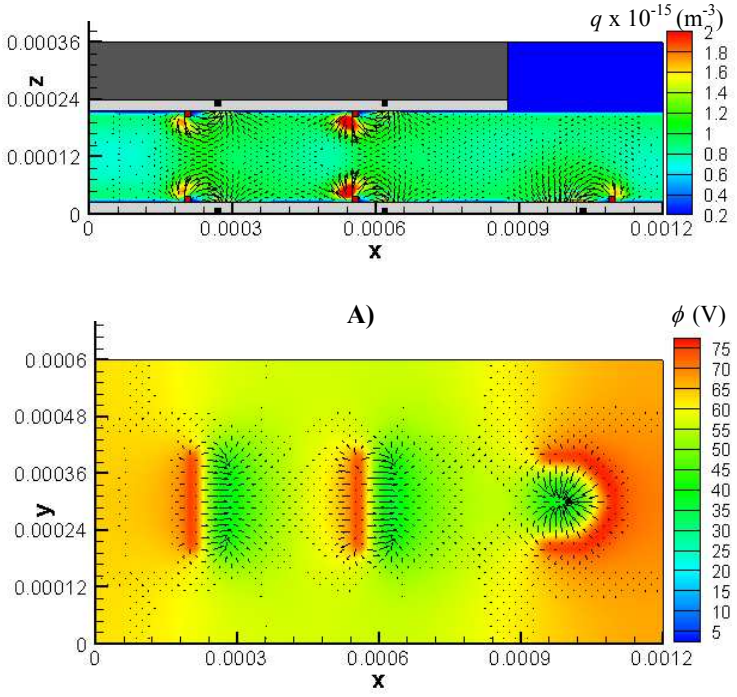

Figure 6. Case#2: A) charge separation $q = n_i - n_e$ at x-z plane (y = 0.3 mm) and B) potential distribution at x-y plane (z = 0.03 mm) with force vectors.

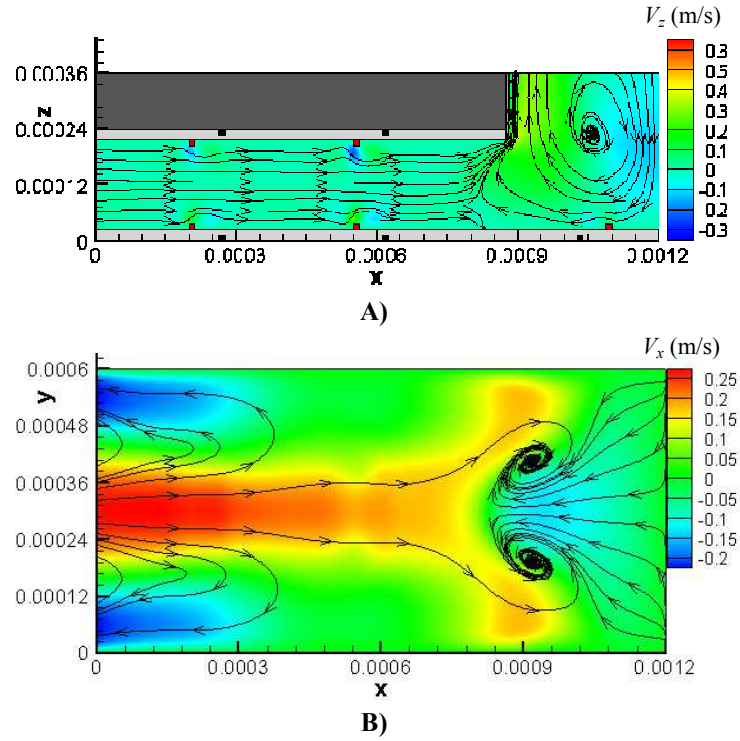

Figure 7. Case#2: A) V_z-velocity contour at x-z plane (y = 0.3 mm) and B) V_x-velocity contour at x-y plane (z = 0.12 mm) with streamtraces.

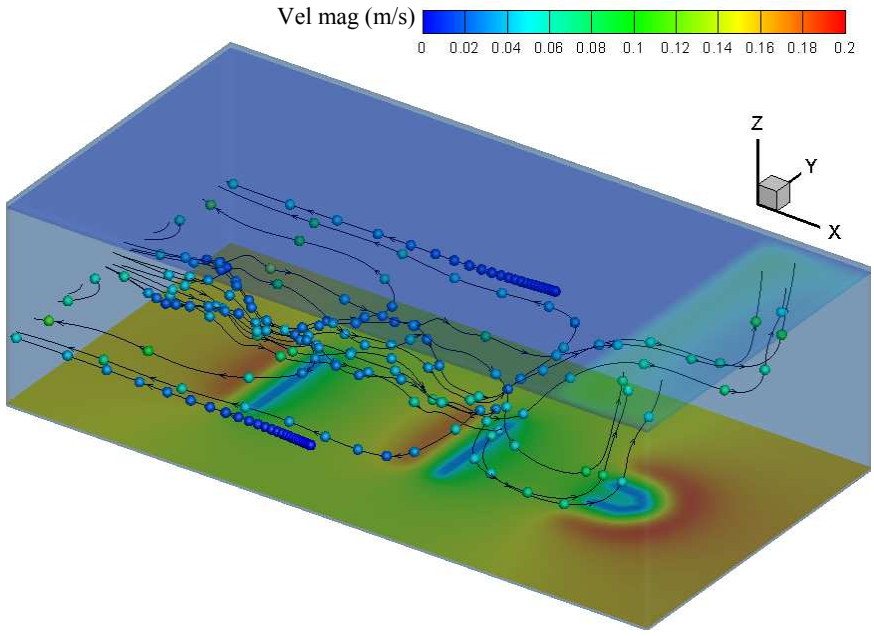

A)

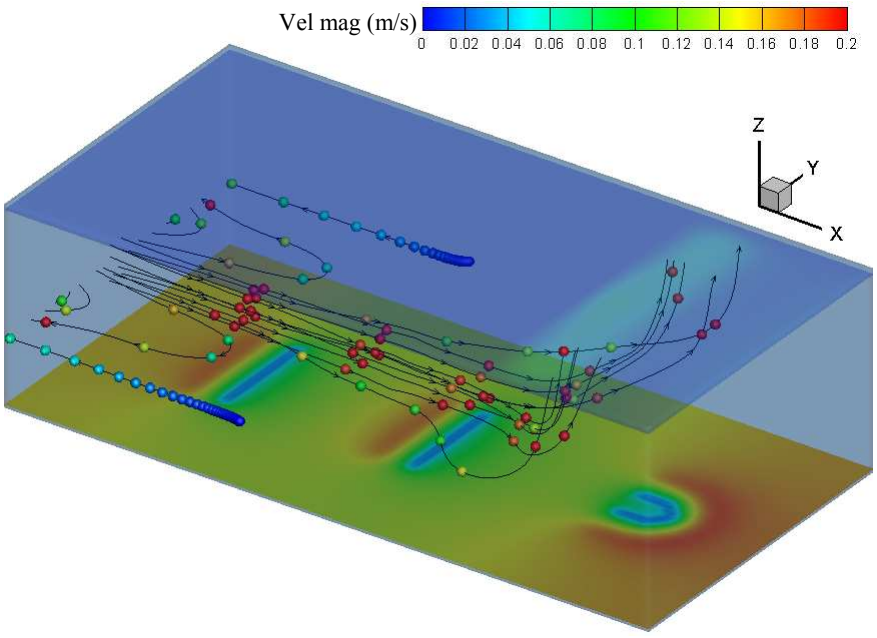

B)

Figure 8. Fluid particles and top wall colored with velocity magnitude; bottom wall colored with potential for A) Case#1 and B) Case#2.